Research Article | Vol. 27, No. 26 / 23 December 2019 / Optics Express 37634
Optics EXPRESS

Advanced iterative algorithm for phase extraction: performance evaluation and enhancement

YUCHI CHEN AND QIAN KEMAO*

School of Computer Science and Engineering, Nanyang Technological University, Singapore 639798, Singapore
*mkmqian@ntu.edu.sg

Abstract: Phase-shifting techniques are extremely important in modern optical metrology. The advanced iterative algorithm (AIA) is an elegant, flexible and effective phase-shifting algorithm that can extract phase from fringe patterns with arbitrary unknown phase-shifts. However, comparing it with traditional phase-shifting algorithms, AIA has not been sufficiently investigated on (i) its applicability to different types of fringe patterns; (ii) its performance with respect to different phase-shifts, frame numbers and noise levels and thus the possibility of further improvement; and (iii) the predictability of its accuracy. To solve these problems, a series of innovations are proposed in this paper. First, condition numbers are introduced to characterize the least squares matrices used in AIA, and subsequently a fringe density requirement is suggested for the success of AIA. Second, the performance of AIA regarding different phase-shifts, frame numbers and noise levels is thoroughly evaluated by simulations, based on which, an overall phase error model is established. With such understanding, three individual improvements of AIA, i.e., controlling phase-shifts, controlling frame numbers and suppressing noise, are proposed for better performance of AIA. Third, practical methods for estimating the overall phase errors are developed to make the AIA performance predictable even before AIA is executed. We then integrate all these three innovations into an enhanced AIA (eAIA), which solves all the problems we mentioned earlier. The significant contributions of eAIA include the insurability of the convergence, the controllability of the performance, and achievability of a desired accuracy. An experiment is carried out to demonstrate the effectiveness of eAIA.

1. Introduction

Phase-shifting interferometry has been widely used to precisely measure physical quantities such as shape, deformation and refractive index [1–3]. Phase-shifted fringe patterns can be represented as [4]

$$I_{ij}^{t} = A_{ij} + B_{ij}\cos(\varphi_j + \delta_i), i = 1, 2, \ldots, M; j = 1, 2, \ldots, N, \tag{1}$$

where the subscript i represents the i^{th} fringe pattern with M as the total number of fringe patterns; the subscript j represents the j^{th} pixel with N as the total number of pixels; I_{ij}^{t} is the theoretical fringe intensity; A_{ij} and B_{ij} represent the background intensity and fringe amplitude, respectively; φ_j is the phase information of the j^{th} pixel and is assumed to be independent of i; and δ_i is the phase-shift of the i^{th} frame with $\delta_1 = 0$, and is assumed to be independent of j. Among these variables, the phase information φ_j is directly related to the measured quantities [1–3] and thus need to be extracted from fringe patterns. In practice, as noise is unavoidable, the measured fringe patterns are normally presented as

$$I_{ij} = I_{ij}^{t} + n_{ij}, \tag{2}$$

where n_{ij} is the noise of the j^{th} pixel at i^{th} fringe pattern.

#378998 https://doi.org/10.1364/OE.27.037634
Journal © 2019 Received 26 Sep 2019; revised 18 Nov 2019; accepted 27 Nov 2019; published 12 Dec 2019

Optics EXPRESS

Due to the extreme importance of phase extraction, many phase-shifting algorithms have been developed. Based on the prior knowledge about the phase-shifts, they can be classified into two categories [4]:

(i) Algorithms with known phase-shifts: the least square algorithm (LSA) [1], the N + 1 bucket algorithm [5] and the windowed digital Fourier transform algorithms [6] are such examples. Performance evaluation of these algorithms is relatively easy and has been intensively carried out [6–9];

(ii) Algorithms with unknown phase-shifts: the Carre's algorithm [10], the Hariharan algorithm [11], the advanced iterative algorithm (AIA) [12], the algorithms based on principal component analysis [13], Euclidean matrix norm [14] and Gram–Schmidt orthonormalization [15] belong to this category. Naturally, the unknown phase-shifts bring uncertainty and challenge for performance evaluation.

Among all these algorithms, AIA is of particular interest to us. AIA iteratively estimates the phase and phase-shifts until the stopping criterion is satisfied. It offers the following merits: (i) the algorithmic simplicity and elegance, (ii) the flexibility of using arbitrary phase-shifts, and frame numbers ($\geq$3), and (iii) the good performance demonstrated in the literature and our own testing. However, we also noticed that there is a lack of comprehensive algorithm analysis and performance evaluation with respect to (w.r.t) different phase distributions, phase-shifts, frame numbers, and noise, which leaves an obstacle for using AIA in industrial applications. Specifically, the following aspects of the AIA performance are unclear and should be answered: (i) Is AIA applicable to any set of phase-shifted fringe patterns and successfully converge? (ii) How is the performance affected by different phase-shifts, frame numbers and noise levels, and can the performance be further improved? (iii) Can the accuracy of AIA be predicted? These questions motivate us to investigate the AIA's performance thoroughly, through which we can answer all these questions and propose various improvements accordingly. Finally, by integrating all our findings and solutions, an enhanced AIA (eAIA) is proposed.

The rest of the paper is arranged as follows. In Section 2, the AIA is briefly described and analyzed. Condition numbers are introduced to characterize the least squares matrices used in AIA. In Section 3, simulations of fringe patterns to evaluate AIA are set up. The requirement on fringe density for the effective use of AIA is also obtained and suggested. In Section 4, the performance of AIA w.r.t different variables is thoroughly evaluated, resulting in an integrated general error model. In Section 5, individual improvements w.r.t. different variables in AIA are proposed. In Section 6, practical error estimation methods are proposed to predict the performance of AIA for a given set of phase-shifted fringe patterns. In Section 7, the eAIA is finally proposed and verified in an experiment. Section 8 concludes the paper.

2. Advanced iterative algorithm (AIA) and its analysis

In this section, the AIA is described and analyzed. For clarity, the representations and symbols largely follow the original AIA in [12].

2.1. Algorithm description

AIA iteratively estimates phase and phase-shifts, until a convergence condition is satisfied. First, the phase is estimated by treating the phase-shifts as known; and both fringe background and amplitude are assumed to be constant across frames. Equation (1) is then rewritten as

$$I_{ij}^{t} = a_j + b_j \cos\delta_i + c_j \sin\delta_i, \tag{3}$$

Optics EXPRESS

where $a_j = A_{ij}$; $b_j = B_{ij}\cos\varphi_j$ and $c_j = -B_{ij}\sin\varphi_j$. The following loss function between the measured intensity I_{ij} and the theoretical model I^t_{ij} should be minimized in the least squares sense:

$$S_j = \sum_{i=1}^{M}(I^t_{ij} - I_{ij})^2 = \sum_{i=1}^{M}(a_j + b_j\cos\delta_i + c_j\sin\delta_i - I_{ij})^2. \tag{4}$$

Letting $\frac{\partial S_j}{\partial a_j} = \frac{\partial S_j}{\partial b_j} = \frac{\partial S_j}{\partial c_j} = 0$ yields:

$$\mathbf{A}_{\mathrm{p}}\mathbf{X}_{\mathrm{p},j} = \mathbf{B}_{\mathrm{p},j}, \tag{5}$$

where

$$\mathbf{A}_{\mathrm{p}} = \begin{bmatrix} M & \sum_{i=1}^{M}\cos\delta_i & \sum_{i=1}^{M}\sin\delta_i \\ \sum_{i=1}^{M}\cos\delta_i & \sum_{i=1}^{M}\cos^2\delta_i & \sum_{i=1}^{M}\cos\delta_i\sin\delta_i \\ \sum_{i=1}^{M}\sin\delta_i & \sum_{i=1}^{M}\cos\delta_i\sin\delta_i & \sum_{i=1}^{M}\sin^2\delta_i \end{bmatrix}, \tag{6}$$

$\mathbf{X}_{\mathrm{p},j} = \begin{bmatrix} a_j & b_j & c_j \end{bmatrix}^T$, and $\mathbf{B}_{\mathrm{p},j} = \begin{bmatrix} \sum_{i=1}^{M} I_{ij} & \sum_{i=1}^{M} I_{ij}\cos\delta_i & \sum_{i=1}^{M} I_{ij}\sin\delta_i \end{bmatrix}^T$. It is clear that $\mathbf{A}_{\mathrm{p}}$ is a function of phase-shifts. If $\mathbf{A}_{\mathrm{p}}$ is nonsingular, we have

$$\mathbf{X}_{\mathrm{p},j} = \mathbf{A}_{\mathrm{p}}^{-1}\mathbf{B}_{\mathrm{p},j}, \tag{7}$$

where the subscript -1 indicates the matrix inverse. Subsequently, the phase can be extracted as

$$\varphi_j = \tan^{-1}\left(-\frac{c_j}{b_j}\right). \tag{8}$$

Similarly, the phase-shifts are estimated by treating the phases of all pixels as known and both fringe background and amplitude are assumed to be constant across pixels in each frame. Equation (1) is then rewritten as

$$I^t_{ij} = a'_i + b'_i\cos\varphi_j + c'_i\sin\varphi_j, \tag{9}$$

where $a'_i = A_{ij}$; $b'_i = B_{ij}\cos\delta_i$ and $c'_i = -B_{ij}\sin\delta_i$. The following loss function between the measured intensity I_{ij} and the theoretical model I^t_{ij} should be minimized in the least squares sense:

$$S'_i = \sum_{j=1}^{N}(I^t_{ij} - I_{ij})^2 = \sum_{j=1}^{N}(a'_i + b'_i\cos\varphi_j + c'_i\sin\varphi_j - I_{ij})^2. \tag{10}$$

Letting $\frac{\partial S'_i}{\partial a'_i} = \frac{\partial S'_i}{\partial b'_i} = \frac{\partial S'_i}{\partial c'_i} = 0$ yields:

$$\mathbf{A}_{\mathrm{ps}}\mathbf{X}_{\mathrm{ps},i} = \mathbf{B}_{\mathrm{ps},i}, \tag{11}$$

where

$$\mathbf{A}_{\mathrm{ps}} = \begin{bmatrix} N & \sum_{j=1}^{N}\cos\varphi_j & \sum_{j=1}^{N}\sin\varphi_j \\ \sum_{j=1}^{N}\cos\varphi_j & \sum_{j=1}^{N}\cos^2\varphi_j & \sum_{j=1}^{N}\cos\varphi_j\sin\varphi_j \\ \sum_{j=1}^{N}\sin\varphi_j & \sum_{j=1}^{N}\cos\varphi_j\sin\varphi_j & \sum_{j=1}^{N}\sin^2\varphi_j \end{bmatrix}, \tag{12}$$

$\mathbf{X}_{\mathrm{ps},i} = \begin{bmatrix} a'_i & b'_i & c'_i \end{bmatrix}^T$ and $\mathbf{B}_{\mathrm{ps},i} = \begin{bmatrix} \sum_{j=1}^{N} I_{ij} & \sum_{j=1}^{N} I_{ij}\cos\varphi_j & \sum_{j=1}^{N} I_{ij} & \sin\varphi_j \end{bmatrix}^T$. The $\mathbf{A}_{\mathrm{ps}}$ is a function of phase distribution. If $\mathbf{A}_{\mathrm{ps}}$ is nonsingular, we have

$$\mathbf{X}_{\mathrm{ps},i} = \mathbf{A}_{\mathrm{ps}}^{-1}\mathbf{B}_{\mathrm{ps},i}, \tag{13}$$

Optics EXPRESS

from which, the phase-shifts are calculated,

$$\delta_i = \tan^{-1}\left(-\frac{c_i'}{b_i'}\right). \tag{14}$$

The above phase calculation and phase-shifts calculation are iteratively executed. AIA starts with random guessed phase-shifts and stops when the following condition is satisfied for all i:

$$|(\delta_i^k - \delta_1^k) - (\delta_i^{k-1} - \delta_1^{k-1})| < \varepsilon, \tag{15}$$

where ε is a pre-set error tolerance and the superscript k is the number of iteration.

2.2. Condition numbers of least squares matrices

As can be seen from Eqs. (7) and (13), the performance of AIA directly relies on the two least squares matrices $\mathbf{A}_\mathrm{p}$ and $\mathbf{A}_\mathrm{ps}$, thus phase distribution and phase-shifts. AIA works poorly when $\mathbf{A}_\mathrm{p}$ and $\mathbf{A}_\mathrm{ps}$ are singular or nearly singular. Since condition number is a good indicator of matrix singularity [16], we propose to adopt it to qualify these matrices. Given a linear equation system $\mathbf{Hx} = \mathbf{F}$, the condition number of matrix $\mathbf{H}$ is calculated as follows [17],

$$\kappa(\mathbf{H}) = \frac{\sigma_{\max}(\mathbf{H})}{\sigma_{\min}(\mathbf{H})}, \tag{16}$$

where $\sigma_{\min}(\mathbf{H})$ and $\sigma_{\max}(\mathbf{H})$ are the minimal and maximal singular values of $\mathbf{H}$, respectively.

Consider matrix $\mathbf{A}_\mathrm{ps}$ first. For any vector $\mathbf{x}$ with real components, the dot product of $\mathbf{A}_\mathrm{ps}\mathbf{x}$ and $\mathbf{x}$ is

$$\langle \mathbf{A}_\mathrm{ps}\mathbf{x}, \mathbf{x} \rangle = \mathbf{x}^T\mathbf{A}_\mathrm{ps}\mathbf{x} = \sum_{j=1}^{N} (x_1 + \cos\varphi_j x_2 + \sin\varphi_j x_3)^2 \geq 0, \tag{17}$$

which implies that $\mathbf{A}_\mathrm{ps}$ is positive semidefinite [17]. Since $\mathbf{A}_\mathrm{ps}$ is a symmetrical positive semidefinite real matrix, based on the property of the Rayleigh quotient [18] and the fact that eigenvalues of $\mathbf{A}_\mathrm{ps}$ equal to its singular values [17], for any vector $\mathbf{x}$ with nonzero real component, we have,

$$\sigma_{\min}(\mathbf{A}_\mathrm{ps}) \leq \frac{\mathbf{x}^T\mathbf{A}_\mathrm{ps}\mathbf{x}}{\mathbf{x}^T\mathbf{x}} \leq \sigma_{\max}(\mathbf{A}_\mathrm{ps}). \tag{18}$$

Substituting different values of $\mathbf{x}$, e.g. $\begin{bmatrix} 1 & 0 & 0 \end{bmatrix}^T$, $\begin{bmatrix} 0 & 1 & 0 \end{bmatrix}^T$ and $\begin{bmatrix} 0 & 0 & 1 \end{bmatrix}^T$, into Eq. (18) yields

$$\sigma_{\max}(\mathbf{A}_\mathrm{ps}) \geq N, \tag{19}$$

$$\sigma_{\min}(\mathbf{A}_\mathrm{ps}) \leq \min\left(\sum_{j=1}^{N}\cos^2\varphi_j, \sum_{j=1}^{N}\sin^2\varphi_j\right). \tag{20}$$

Thus following Eq. (16), we have

$$\kappa(\mathbf{A}_\mathrm{ps}) \geq \frac{N}{\min\left(\sum_{j=1}^{N}\cos^2\varphi_j, \sum_{j=1}^{N}\sin^2\varphi_j\right)}. \tag{21}$$

Based on Pythagorean trigonometric identity,

$$\cos^2\varphi + \sin^2\varphi = 1, \tag{22}$$

it is not difficult to find that

$$\min\left(\sum_{j=1}^{N}\cos^2\varphi_j, \sum_{j=1}^{N}\sin^2\varphi_j\right) \leq \frac{N}{2}. \tag{23}$$

Hence the inequality Eq. (21) becomes

$$\kappa(\mathbf{A}_\mathrm{ps}) \geq 2, \tag{24}$$

where $\kappa(\mathbf{A}_\mathrm{ps}) = 2$ is achievable when $\sigma_{\min}(\mathbf{A}_\mathrm{ps}) = \sum_{j=1}^{N}\cos^2\varphi_j = \sum_{j=1}^{N}\sin^2\varphi_j = \frac{N}{2}$, i.e., the phase evenly distributed among 2π. In the meantime, $\mathbf{A}_\mathrm{ps}$ could be singular in special cases, e.g. $\varphi_j = 0$,

Optics EXPRESS

for $j = 1, 2, \ldots, N$. Thus, we have $2 \leq \kappa(\mathbf{A}_{\mathrm{ps}}) < \infty$. Similarly, we also have $2 \leq \kappa(\mathbf{A}_{\mathrm{p}}) < \infty$, where $\kappa(\mathbf{A}_{\mathrm{p}}) = 2$ is achievable when $\delta_i = (i\text{-}1) \times 2\pi/M$.

3. Fringe pattern simulation and fringe density requirement for AIA

In this section, the fringe pattern simulation strategies which are used throughout the paper are introduced first. Based on simulations, a fringe density requirement for using AIA is established.

3.1. Fringe pattern simulation

Our main tool for AIA evaluation in this paper is simulation, which provides us the ground true values for comparison and enables us to run tests thousands of times easily. Nevertheless, an experimental example will be provided at the end of the paper.

The fringe patterns are simulated according to Eq. (2) with the following settings:

(i) $M = 3 \sim 40$;

(ii) $N = N_x$ (horizontal) $\times N_y$ (vertical) $= 256 \times 256$;

(iii) the background intensity A and fringe amplitude B are constant across both frames and pixels;

(iv) three typical phase distributions, linear for straight fringe patterns (φ^1), quadratic for circular fringe patterns (φ^2), and a "peaks" function for complex fringe patterns (φ^3), are used as represented below,

$$\varphi^1(x, y) = \frac{2N_p\pi}{N_x}x, \tag{25}$$

$$\varphi^2(x, y) = \frac{2N_p\pi}{\left(\frac{N_x}{2}\right)^2 + \left(\frac{N_y}{2}\right)^2}r^2, \tag{26}$$

$$\varphi^3(x, y) = N_p \times \mathrm{peaks_s}(N_x, N_y) + \omega_c x \tag{27}$$

where N_p is number of fringes over ROI, $r^2 = \left(x - \frac{N_x}{2}\right)^2 + \left(y - \frac{N_y}{2}\right)^2$, "peaks_s" uses the MATLAB function "peaks", linearly scaled it into the range of $[0, 2\pi]$ and ω_c represents the carrier frequency;

(v) phase-shifts are either randomly drawn from $[0, 2\pi]$ or specially set as $\delta_i = (i\text{-}1) \times 2\pi/M$ so that $\kappa(\mathbf{A}_{\mathrm{ps}})$ is minimal;

(vi) additive white noises have a zero mean and different standard deviations relative to the fringe amplitude B, i.e., $\sigma/B = 0\% \sim 100\%$ [19].

As examples, a noiseless straight fringe pattern with $N_p = 1$, a circular fringe pattern with $N_p = 2$ and additive noise with $\sigma/B = 10\%$ and a complex fringe pattern with $N_p = 3$, $\omega_c = 0$ and additive noise with $\sigma/B = 20\%$ are shown in Figs. 1(a)–1(c), respectively.

3.2. Fringe density requirement

AIA is not a panacea that can work with any set of fringe patterns. If the fringe patterns have low density, the $\mathbf{A}_{\mathrm{ps}}$ will be singular or nearly singular, making AIA simply fail. Finding the requirement of fringe density to make AIA successful is our first task.

Two groups of fringe patterns are simulated according to Section 3.1 with $M = 4$; phase-shifts are specially set as $\delta_i = (i\text{-}1) \times 2\pi/M$; $N_p = 0.1 \sim 3$ for φ^1, φ^2 and φ^3 and $\omega_c = 0$ for φ^3; $\sigma/B = 0\%$ for noiseless group and $\sigma/B = 10\%$ for noisy group. Both groups of simulations are repeated for

Optics EXPRESS

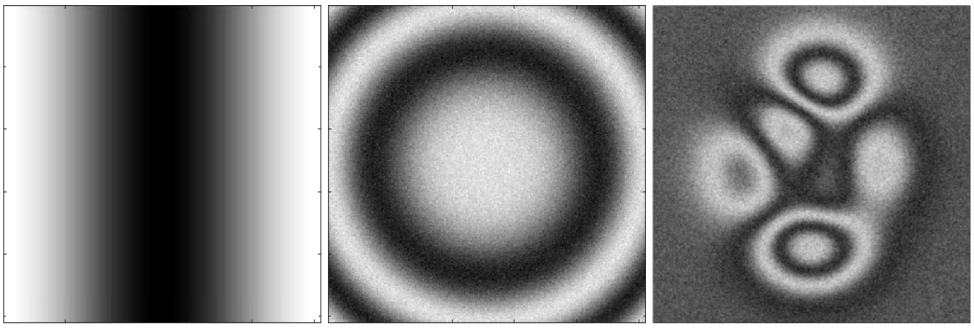

(a) (b) (c)

Fig. 1. Typical fringe patterns used for simulation. (a) A noiseless straight fringe pattern with $N_p = 1$. (b) A circular fringe pattern with $N_p = 2$ and additive noise with $\sigma/B = 10\%$. (c) A complex fringe pattern with $N_p = 3$ and $\omega_c = 0$ and additive white noise with $\sigma/B = 20\%$

1,000 times to reduce the influence of randomly guessed initial phase-shift values. The phases are calculated by AIA from these fringe patterns, where AIA is coded according to Section 2.1 with an error tolerance of 1e-4 rad. The $\kappa(\mathbf{A}_{\text{ps}})$ of these fringe patterns are plotted against N_p in Fig. 2(a). Since the mean phase error is not significantly smaller than the standard deviation in AIA, the root-mean-square error (RMSE) is chosen as a convenient phase error measure and used throughout this paper. Here, the maximum RMSEs of the phases of fringe patterns with different N_p values are calculated and plotted in Figs. 2(b) and 2(c) for noiseless and noisy cases, respectively. From these results, we consider $N_p = 0.5$ as a critical point of AIA performance. When $N_p < 0.5$, $\mathbf{A}_{\text{ps}}$ is nearly singular, and the performance of AIA cannot be guaranteed in both noiseless and noisy tests. Conservatively, we suggest capturing at least one fringe over ROI (i.e., $N_p \geq 1$) as the fringe density requirement for using AIA so that $\kappa(\mathbf{A}_{\text{ps}})$ approaches 2 to achieve good performance. We then further generate a total of 60,000 sets of fringe patterns satisfying the fringe density requirement, i.e., $N_p \geq 1$, and test AIA on them. All tests converge. We thus consider our suggested fringe density requirement valid and will satisfy this requirement in the rest of the paper.

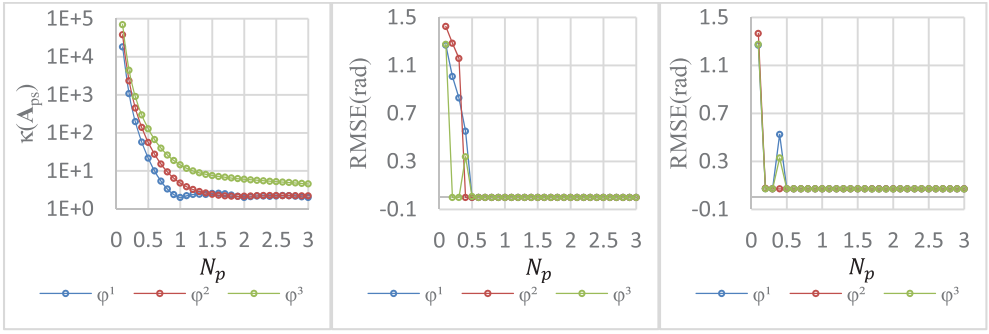

(a) (b) (c)

Fig. 2. Fringe density requirement. (a) $\kappa(\mathbf{A}_{\text{ps}})$ of φ^1, φ^2 and φ^3 w.r.t N_p. (b) RMSEs of phases from noiseless fringe pattern with φ^1, φ^2 and φ^3 w.r.t N_p. (c) RMSEs of phases from noisy fringe pattern with φ^1, φ^2 and φ^3 w.r.t N_p.

Optics EXPRESS

4. Performance evaluation of AIA

In this section, the performance of AIA w.r.t phase-shifts, frame numbers and noise will be evaluated separately, based on which, an integrated error model for AIA is obtained.

4.1. Influence of phase-shifts

Since the phase-shifts can be characterized by the $\kappa(\mathbf{A}_\mathrm{p})$, we examine how $\kappa(\mathbf{A}_\mathrm{p})$ affects the AIA performance. The fringe patterns are simulated according to Section 3.1 with $M = 4$; $N_p = 1$ for φ^1, $N_p = 2$ for φ^2 and $N_p = 10$ and $\omega_c = 0.25$ for φ^3 to satisfy the phase requirement with $\kappa(\mathbf{A}_\mathrm{ps}) \approx 2$; random phase-shifts with $\kappa(\mathbf{A}_\mathrm{p}) = 2 \sim 500$; and $\sigma/B = 10\%$. One fringe pattern with φ^3 is shown in the Fig. 3 as an example.

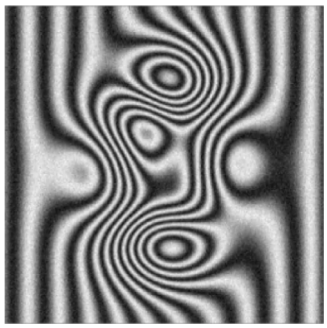

Fig. 3. A complex fringe pattern with φ^3 ($N_p = 10$ and $\omega_c = 0.25$) as phase and additive white noise with $\sigma/B = 10\%$

Phases are then calculated by AIA and LSA with the simulated known phase-shifts [1]. The RMSEs of φ^3 by both AIA and LSA w.r.t $\kappa(\mathbf{A}_\mathrm{p})^{1/2}$ are shown in Fig. 4(a), where $\kappa(\mathbf{A}_\mathrm{p})^{1/2}$ have been grouped into different bins with a bin size of 1. The mean values of RMSEs in Fig. 4(a) are also calculated and plotted against mean value of $\kappa(\mathbf{A}_\mathrm{p})^{1/2}$ in Fig. 4(b), where a linear relationship between RMSE and $\kappa(\mathbf{A}_\mathrm{p})^{1/2}$ is observed. As expected, a smaller $\kappa(\mathbf{A}_\mathrm{p})$ is desired for a better performance of AIA. AIA without the knowledge of the phase-shifts has a comparable performance to LSA with known phase-shifts. More interestingly, the performance

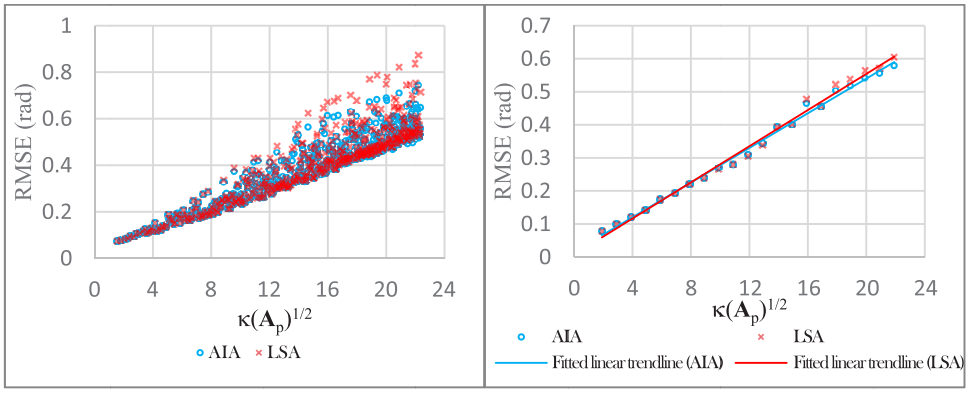

(a) (b)

Fig. 4. Influence of phase-shifts. (a) RMSEs of phases w.r.t $\kappa(\mathbf{A}_\mathrm{p})^{1/2}$. (b) Mean RMSEs of phases w.r.t $\kappa(\mathbf{A}_\mathrm{p})^{1/2}$.

Optics EXPRESS

of AIA could even be slightly better when $\kappa(\mathbf{A}_\mathrm{p})^{1/2} > 10$, which is an interesting point for future investigation. Readers may note that the results of φ^1 and φ^2 are not shown. This is because they are very similar to the result of φ^3. We mention in advance that the same phenomenon will happen in all the rest of the simulations, showing that the AIA performance is insensitive to different types of fringe patterns, as long as the fringe density requirement is satisfied. We thus highlight that, in the rest of the paper, we test all three phase distributions, but only the results of φ^3 are illustrated by default without specification.

4.2. Influence of frame number

We now look at the frame number M. The fringe patterns are simulated according to Section 3.1 with $N_p = 1$ for φ^1, $N_p = 2$ for φ^2 and $N_p = 10$ and $\omega_c = 0.25$ for φ^3; the phase-shifts set as δ_i=(i-1)×2π/M; and $\sigma/B = 10\%$. The corresponding RMSEs of phases extracted by AIA are calculated and plotted against M and $M^{-1/2}$ in Figs. 5(a) and 5(b), respectively. The RMSE decreases w.r.t M and increases linearly w.r.t $M^{-1/2}$, meaning that using more phase-shifted fringe patterns is benificial.

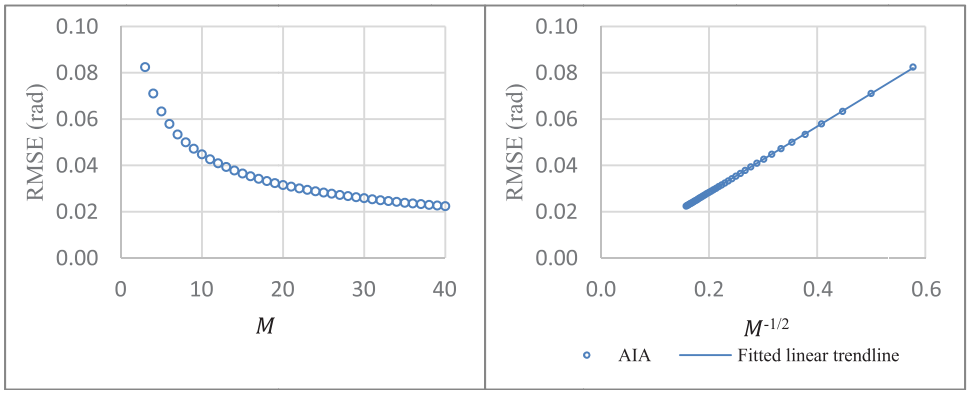

(a) (b)

Fig. 5. Influence of frame number. (a) RMSEs of phases w.r.t M. (b) RMSEs of phases w.r.t $M^{-1/2}$.

4.3. Influence of noise

In AIA, noise affects $\mathbf{B}_{\mathrm{p},i}$ in Eq. (7) and $\mathbf{B}_{\mathrm{ps},i}$ in Eq. (13), and consequently affects the phase extraction accuracy. The fringe patterns are simulated according to Section 3.1 with $M = 4$; $N_p = 1$ for φ^1, $N_p = 2$ for φ^2 and $N_p = 10$ and $\omega_c = 0.25$ for φ^3; and δ_i=(i-1)×2π/M. RMSEs of phases extracted by AIA is plotted against σ/B as shown in Fig. 6. The RMSE linearly increases w.r.t σ.

4.4. The integrated general error model of AIA

Similar relationships between RMSEs with M and σ have been found in non-iterative algorithms [8,20,21], but are introduced for the first time in the context of AIA. These relationships between RMSEs with $\kappa(\mathbf{A}_\mathrm{p})$, M and σ motivated us to fit an integrated general error model for AIA (E_AIA) as follow:

$$E_\mathrm{AIA} = 0.42\left(\sqrt{\kappa(\mathbf{A}_\mathrm{p})} + 2\right) \times \frac{\sigma/B}{\sqrt{M}} \tag{28}$$

To verify the error model, fringe patterns are simulated according to Section 3.1 with $M = 3 \sim 10$; random phase-shifts with $\kappa(\mathbf{A}_\mathrm{p}) = 2 \sim 50$; $N_p = 1$ for φ^1, $N_p = 2$ for φ^2 and $N_p = 10$ and $\omega_c = 0.25$

Optics EXPRESS

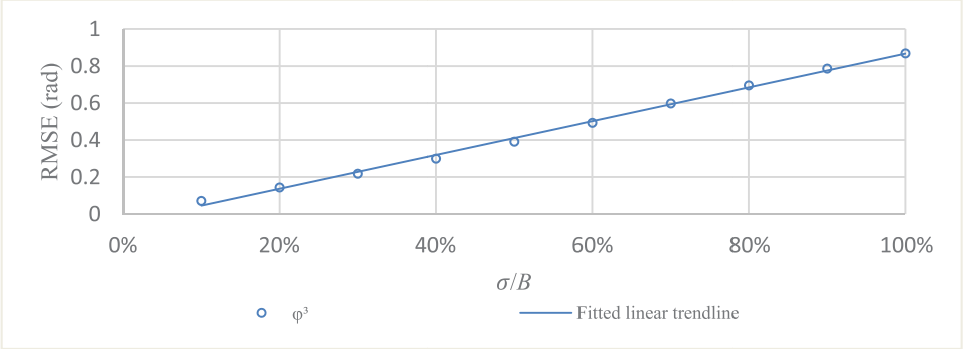

Fig. 6. RMSE of phases w.r.t σ/B.

for φ^3; and $\sigma/B = 10\% \sim 50\%$. The RMSEs of phases are calculated and plotted against E_{AIA} in Fig. 7. Excellent agreement is observed, and thus E_{AIA} can be used as an indicator for accuracy of the phase calculated by AIA.

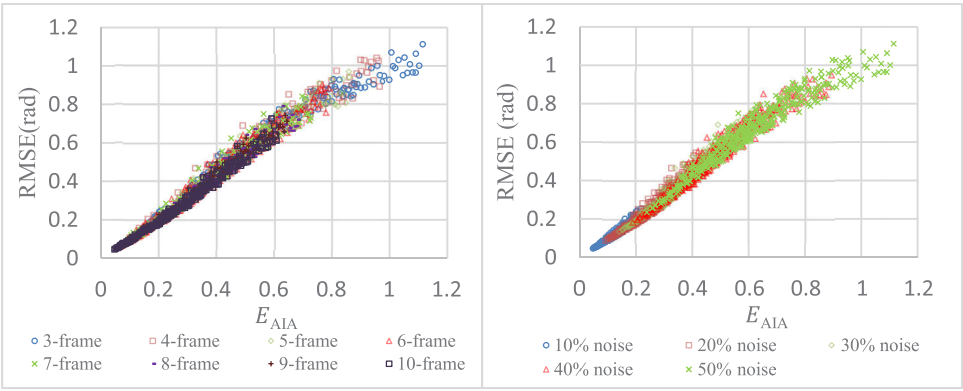

(a) (b)

Fig. 7. Error model validation. (a) RMSEs of phases w.r.t E_{AIA} with different M. (b) RMSEs of phases w.r.t E_{AIA} with different σ/B.

5. Improvements of AIA

The above section shows the relationships between the accuracy of AIA with $\kappa(\mathbf{A}_{\mathrm{p}})$, M and σ. In this section, we turn to improve the performance of AIA by reducing σ or $\kappa(\mathbf{A}_{\mathrm{p}})$ or increasing M.

5.1. Improvement by phase-shifts control

The unique advantage of AIA is to extract phase from any randomly phase-shifted fringe patterns. Thus, controlling the phase-shifts has been ignored in the literature. However, as shown in Section 4.1, smaller $\kappa(\mathbf{A}_{\mathrm{p}})$ leads to better performance. Phase-shifts evenly or nearly evenly distributed within $[0, 2\pi]$ result in a small $\kappa(\mathbf{A}_{\mathrm{p}})$, thus leading to better phase accuracy. We propose that phase-shifts control should be the first improvement of AIA, which is practical as it have been widely implemented in phase-shifting interferometry [3]. We highlight that, in contrast to the traditional phase-shifting algorithm, the control of phase-shifts in AIA does not need to be precise.

Optics EXPRESS

For verification, two groups of fringe patterns are simulated as same as in Section 4.1 except that for the controlled group, phase-shifts are set nearly evenly distributed within [0, 2π], simulated as $\delta_i = (i\text{-}1)\times 2\pi/M + n_\delta$ where n_δ is a random phase-shift error with a mean of zero and standard deviation of 5 degree, resulting in $\kappa(\mathbf{A}_p) \approx 2$; while for the random group, phase-shifts are randomly taken from [0, 2π]. Each group includes 1,000 sets of fringe patterns. Then, the phases are extracted by AIA where the initial phase-shifts set as $\delta_i = (i\text{-}1)\times 2\pi/M$ for the controlled group and random values for the random group. The RMSEs of phases are shown in Fig. 8 with the y-axis shown in log scale, which demonstrates the improvement of the accuracy of AIA. In addition, the convergence is also accelerated with the phase-shift control. The average iteration number for the controlled group with $\delta_i = (i\text{-}1)\times 2\pi/M$ as initial phase-shifts is 9.3, compared with 13.3 for the random group with random initial phase-shifts. Both accuracy and speed results clearly show the advantages of using controlled phase-shifts. Thus, using controlled phase-shifts is encouraged in AIA.

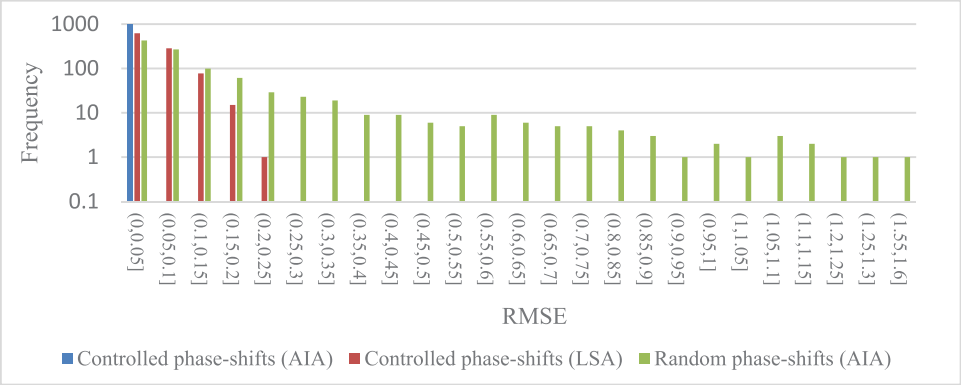

Fig. 8. RMSEs of phases of controlled phase-shifts group and random phase-shifts group.

Furthermore, for the controlled group, we also test LSA for phase extraction using the nominal values of phase-shifts, $\delta_i = (i\text{-}1)\times 2\pi/M$, as true phase-shifts. The RMSE distribution is also inserted in Fig. 8 which is inferior to the AIA result for the same group. It demonstrates the advantage of using AIA when the phase-shift control is not precise, a situation often encountered in real practice [22].

5.2. Improvement by frame number control

When the phase-shifts cannot be well controlled, random phase-shifts between [0, 2π] are expected. Increasing the frame number is useful for decreasing $\kappa(\mathbf{A}_p)$ and proposed as the second improvement of AIA. To verify it, fringe patterns are simulated as same as in Section 4.2 except that $M = 4 \sim 20$ and the phase-shifts are random values between [0, 2π]. There are 1,000 sets of fringe patterns for each frame number. The phases are calculated by AIA. The mean values $\kappa(\mathbf{A}_p)$ and RMSEs of phases with same M are shown in Figs. 9(a) and 9(b), respectively. Both the mean value of $\kappa(\mathbf{A}_p)$ and RMSE decrease w.r.t M. Although we only consider random phase-shifts in this section, increasing frame number with controlled phase-shifts will also improve the accuracy of AIA as shown in Section 4.2.

5.3. Improvement by fringe denoising

Since AIA performs better with lower noise level, we suggest adding a pre-filtering step to the fringe patterns as the third improvement of AIA. In the meantime, pre-filtering should not distort the fringe patterns. Based on these considerations, we selected two filters, a 3×3 median filter

Optics EXPRESS

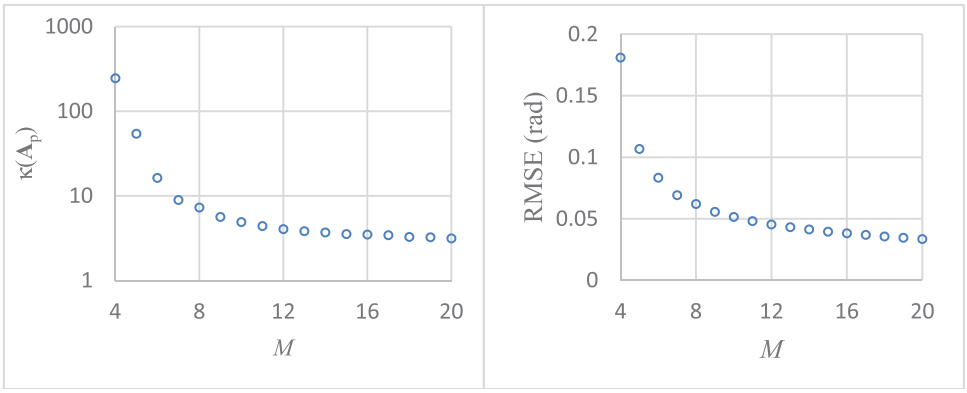

(a) (b)

Fig. 9. Improvement by frame number control. (a) Mean values of $\kappa(\mathbf{A}_p)$ w.r.t M.(b) Mean values of RMSEs of phases w.r.t M.

(MF) for its known simplicity and effectiveness for general images and a windowed Fourier filter (WFF) for its effectiveness for fringe denoising [23]. Fringe patterns are simulated as same as in Section 4.3. Before the phase calculation by AIA, the fringe patterns are filtered by the MF and WFF. The RMSEs of phases calculated by AIA from unfiltered and filtered fringe patterns are plotted against σ/B as shown in Fig. 10. Both MF and WFF significantly improve the accuracy of the phase calculated by AIA. WFF performs better than MF.

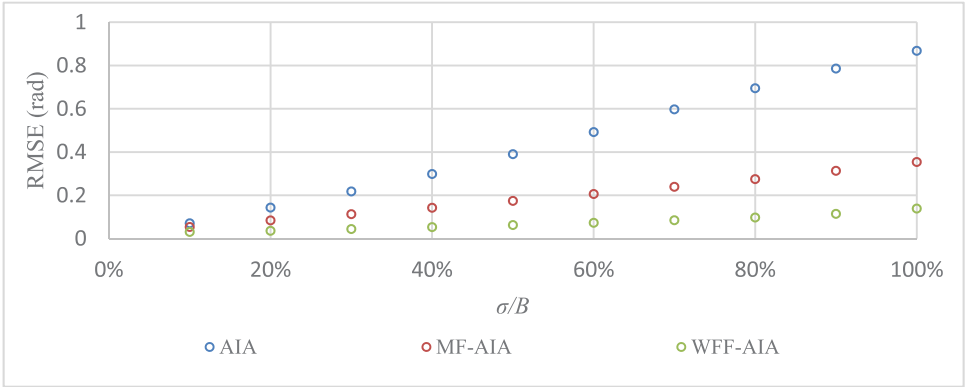

Fig. 10. RMSEs of phases from unfiltered fringe patterns, MF filtered fringe patterns and WFF filtered fringe patterns w.r.t σ/B.

6. Practical error estimation

Although E_{AIA} in Section 4.4 can indicate the performance of AIA, it cannot be directly used in practice, as none of the phase-shifts, noise amplitude and fringe amplitude are known in advance. Estimation of these parameters and subsequently the phase error ($\hat{E}_{\mathrm{AIA}}$) is the main topic of this section.

Optics EXPRESS

6.1. Estimation of phase-shifts

There are multiple phase-shifts estimation methods such as the ellipse fitting method [24] and windowed Fourier ridges (WFR) method [25]. In this paper, we estimate the phase-shifts in the Fourier domain.

First, the fringe pattern expressed by Eq. (1) is rewritten as

$$I_{ij}^{t} = A_{ij} + C_{ij} + C_{ij}^{*}, \tag{29}$$

with

$$C_{ij} = \frac{1}{2} B_{ij} \exp[\mathbf{j}(\varphi_j + \delta_i)] = \frac{1}{2} B_{ij} \exp(\mathbf{j}\delta_i) \exp(\mathbf{j}\varphi_j), \tag{30}$$

where the superscript * is the complex conjugate and $\mathbf{j}$ is an imaginary unit. Since $\delta_1 = 0$, it is clear from Eq. (30),

$$C_{ij} = C_{1j} \exp(\mathbf{j}\delta_i), \tag{31}$$

showing that δ_i can be extracted from C_{ij}.

However, in practice, C_{ij} has to be separated from $C_{i\,j}$* and A_{ij}, for which we rely on the Fourier transform. The 2D Fourier transform of Eq. (29) is

$$F[I(\xi_x, \xi_y; i)] = F[A] + F[C(\xi_x, \xi_y; i)] + F[C^{*}(\xi_x, \xi_y; i)], \tag{32}$$

where ξ_x and ξ_y are the frequency coordinates in the Fourier domain among row and column directions, respectively. Each of the items on the right hand of Eq. (32) gives a spectrum lobe. We identify the spectrum lobe of $F[C(\xi_x, \xi_x; i)]$, and find its ridge as

$$(u, v) = \underset{\xi_x, \xi_y}{arg\,\max} \sum_{i=1}^{M} |F[C(\xi_x, \xi_y; i)]|. \tag{33}$$

Based on Eq. (31), phase-shifts can be estimated as

$$\hat{\delta}_i = \angle F[C(u, v; i)] - \angle F[C(u, v; 1)]. \tag{34}$$

This method is a similar concept to WFR but with a worse estimation accuracy. However, it indeed provides a satisfactory accuracy and fast estimation of phase-shifts. The condition number of the estimated least squares matrix for phase calculation $\kappa(\hat{\mathrm{A}}_{\mathrm{p}})$ can subsequently be calculated from the estimated phase-shifts.

6.2. Estimation of fringe amplitude

The fringe amplitude can be calculated by the LSA [2] or window Fourier ridge method [21]. Since we have just estimated the phase-shifts, we can calculate $\mathbf{A}_{\mathrm{p}}$ and $\mathbf{B}_{\mathrm{p},j}$ used in Eq. (7), and subsequently $\mathbf{X}_{\mathrm{p},j}$ can be computed. The pixel-wise fringe amplitude is calculated as

$$\hat{B}_j = \sqrt{b_j^2 + c_j^2}, \tag{35}$$

and the mean fringe amplitude $\hat{B}$ is then estimated as an average across all pixel,

$$\hat{B} = \frac{1}{N} \sum_{j=1}^{N} \hat{B}_j. \tag{36}$$

Optics EXPRESS

6.3. Estimation of noise standard deviation

The noise standard deviation can be estimated by hardware calibration process [26] or noise estimation algorithms. A modified fast noise estimation algorithm using a 3×3 Laplacian mask is adopted in this work, due to its high speed and satisfactory accuracy [27]. It can estimate the noise standard deviation of an unfiltered or 3×3 MF filtered fringe pattern, as follows,

$$\hat{\sigma}_i = \sqrt{\frac{2}{\pi}} \frac{1}{6(N_x - 2)(N_y - 2)} \sum_{I_i^d} |I_i^d \otimes \mathrm{N}|, \tag{37}$$

where $|\cdot|$ takes the absolute value, $\otimes$ is the convolution operator and N is a convolution kernel,

$$\mathrm{N} = \begin{bmatrix} 1 & -2 & 1 \\ -2 & 4 & -2 \\ 1 & -2 & 1 \end{bmatrix}, \tag{38}$$

and I_i^d is a down sampled image of I_i by skipping adjacent 2 pixel in both x and y direction to reduce influence from neighboring pixels caused by the 3×3 MF. The noise standard deviation of the test is estimated based on the mean noise standard deviation value of all frames,

$$\hat{\sigma} = \frac{1}{M} \sum_{i=1}^{M} \hat{\sigma}_i \tag{39}$$

6.4. Practical overall error estimation

With all the estimated parameters, the overall error of AIA can now be obtained as

$$\hat{E}_{\mathrm{AIA}} = 0.42 \left(\sqrt{\kappa(\hat{\mathbf{A}}_{\mathrm{p}})} + 2 \right) \times \frac{\hat{\sigma}/\hat{B}}{\sqrt{M}}. \tag{40}$$

To verify the effectiveness of the estimation, fringe patterns as same as in Section 4.4 are simulated. The RMSEs of phases have been calculated and plotted against $\hat{\mathrm{E}}_{\mathrm{AIA}}$ as shown in Fig. 11. Excellent agreement is observed. The error model can not only estimate accuracy of AIA, but also be used for fringe pattern parameter control to achieve a desired accuracy, as will be described soon.

In the case that the phase-shifts are controllable, $\delta_i = (i\text{-}1)\times 2\pi/M$ will be used so that $\kappa(\mathbf{A}_{\mathrm{p}}) = 2$. From Eq. (40), we can estimate the required frame number as

$$M = \mathrm{ceil}\left[2 \left(\frac{\hat{\sigma}/\hat{B}}{\tau} \right)^2 \right], \tag{41}$$

where τ is the threshold of $\hat{\mathrm{E}}_{\mathrm{AIA}}$. In order to conservatively and thus safely determine an M value, one may use a smaller τ, or directly increase the M value.

Optics EXPRESS

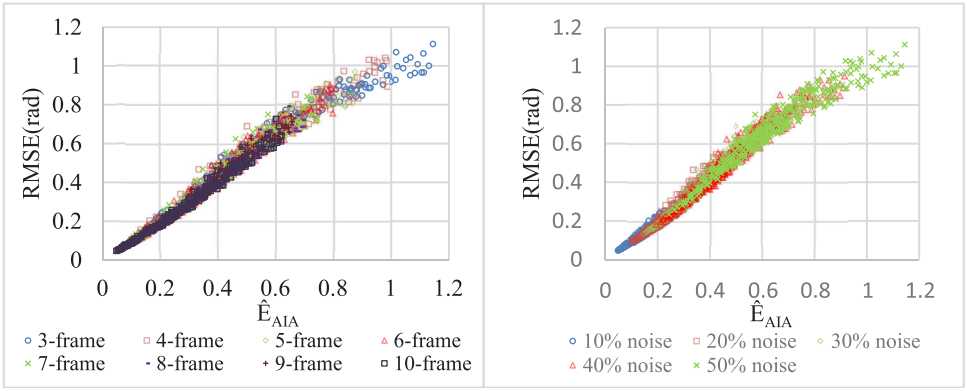

(a) (b)

Fig. 11. Validation of AIA error prediction. (a) RMSEs of phases w.r.t $\hat{E}_{AIA}$ with different M. (b) RMSEs of phases w.r.t $\hat{E}_{AIA}$ with different σ.

7. Enhanced AIA (eAIA)

In this section, based on the fringe density requirement (Section 3.2), the individual improvements of AIA (Section 5) and the practical error estimation (Section 6), eAIA is proposed and verified by an experiment.

7.1. Structure of eAIA

Unlike the traditional phase-shifting algorithms, AIA has higher uncertainty of phase extraction accuracy or could even fail, which is a serious obstacle of practical use. The main feature of the proposed eAIA is the integration of fringe acquisition with phase extraction to guarantee AIA's success with a desired accuracy. The flowchart of eAIA is shown in Fig. 12. The blue, red and green color codes correspond to fringe density requirement, performance improvements and performance prediction, respectively. The detailed highlights are as follows:

(i) AIA has unsatisfactory performance when fringes are sparse. Thus, the fringe density requirements are integrated into eAIA. The fringe density can be increased by adjusting the optical system such as adjusting a mirror. Note that since only one fringe is required in the field of view, the adjustment is very little;

(ii) Although AIA is known for its merits of using arbitrary phase-shifts, controlling phase-shifts makes phase extraction more accurate and faster, and is encouraged. Note that the phase-shift control does not need to be precise, and thus it is easy to implement;

(iii) The error model and its effective estimation enable us to predict the AIA performance, with which, the original AIA system is modified into an adaptive algorithm until a desired accuracy is achieved. Note that this process is recursive without human intervention and thus is automatic.

In Fig. 12, a 3×3 MF is used as the fringe filter due to its high speed, but other filters can also be used if it is effective for denoising and the noise level after filtering can be well estimated.

7.2. Experimental verification of eAIA

To verify the effectiveness of eAIA, we conducted an experiment with a Fizeau interferometer. We used a wedged optical window as the reference and another wedged optical window as the

Optics EXPRESS

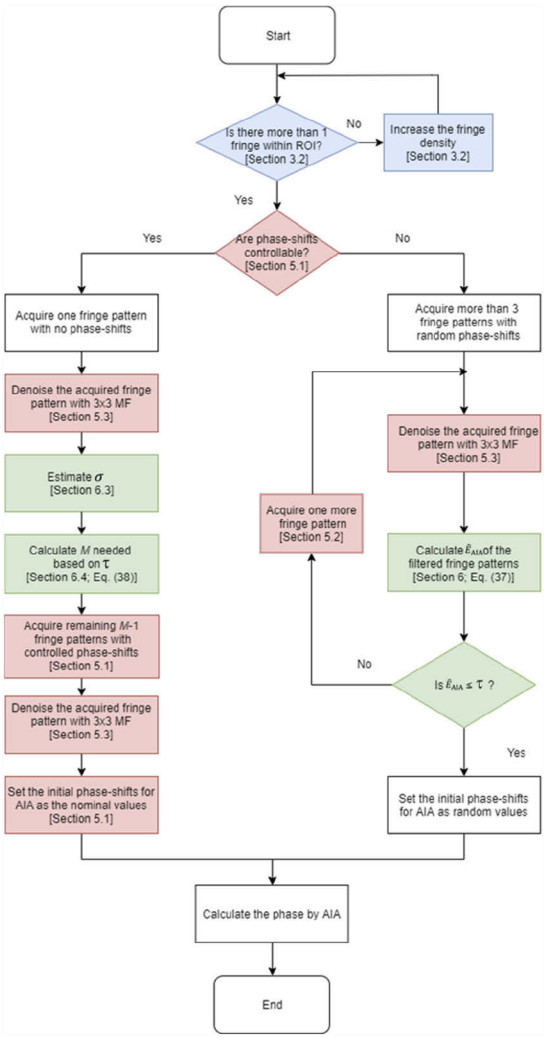

Fig. 12. Flowchart of eAIA.

Optics EXPRESS

test object. In total, 160 fringe patterns with phase-shifts randomly distributed within $[0, 2\pi]$ and an image size of $N = N_x \times N_y = 1000 \times 992$ have been acquired. One of the fringe patterns is shown in Fig. 13(a). AIA is applied to all 160 fringe patterns to extract the phase, as shown in Fig. 13(b). This phase is treated as the ground truth phase of the test object.

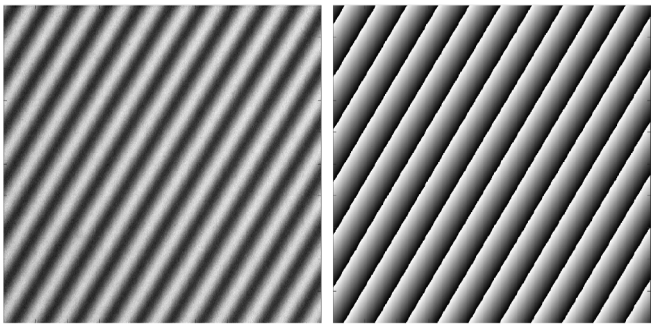

(a) (b)

Fig. 13. Fringe patterns and ground true phase. (a) One of acquired fringe patterns. (b) The ground true phase.

We set the phase-shift of the first fringe pattern as 0 and randomly selected 2 more frames to start eAIA. The accuracy tolerance τ is set as 0.04 rad. The desired phase accuracy is reached when 7 fringe patterns are used. According to the eAIA flowchart, $\hat{E}_{AIA}$ will be calculated when a new fringe pattern is added, but AIA is only applied once in the end. However, to monitor the progress of phase error reduction in this experiment, AIA is also repeatedly applied to fringe patterns. Both $\hat{E}_{AIA}$ and RMSEs of phase calculated by AIA are plotted against frame number in Fig. 14(a). The estimated phase-shifts of the 7 frames are shown in Fig. 14(b) where the bold numbers are the fringe pattern indices. We observe that, (i) using $\hat{E}_{AIA}$ to predict RMSE of phase is effective; (ii) a new fringe pattern with a phase-shift contributing to the evenness of the phase-shift distribution on the unit circle can significantly reduce the phase error. Frames 4 and 5 are such examples; (iii) on the contrary, if a new fringe pattern does not improve the evenness of the phase-shift distribution, the phase error reduction is limited. Frames 6 and 7 are such examples. These observations are valid in our multiple trials with different sets of fringe patterns.

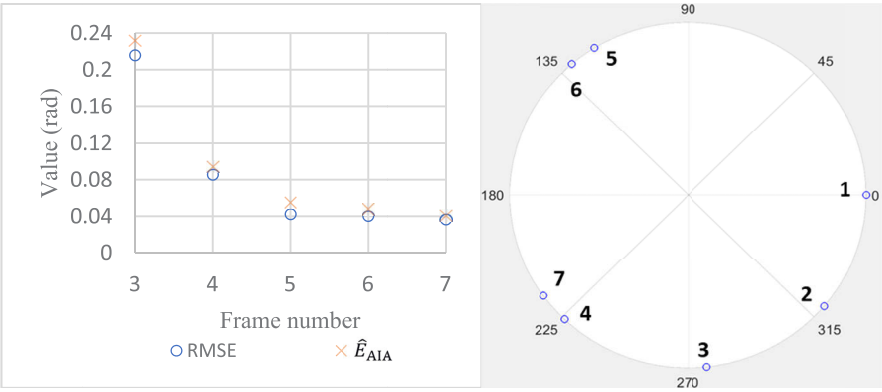

(a) (b)

Fig. 14. Performance of eAIA. (a) RMSE of phases and $\hat{E}_{AIA}$ w.r.t frame number. (b) Estimated phase-shifts of the 7 frames.

Optics EXPRESS

Finally, the phases obtained from eAIA using 3 frames and 7 frames are shown in Figs. 15(a) and 15(b), respectively, which visually show the improvement of the phase quality.

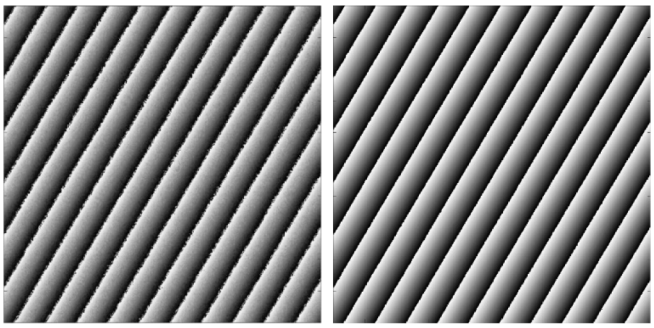

(a) (b)

Fig. 15. Phase calculated with different number of frames. (a) Phase calculated with 3 frames. (b) Phase calculated with 7 frames.

The proposed eAIA is suitable for interferometers with inaccurate phase-shifts or unknown phase-shifts. It provides possibility to extract phase even without the phase-shifts calibrations processes of interferometers.

8. Conclusions

Advanced Iterative Algorithm (AIA) as an elegant, flexible, effective and convenient algorithm which can extract phase from fringe patterns with arbitrary unknown phase-shifts. However, it was confronted with (i) unknown capability in dealing with different types of fringe patterns, (ii) unknown performance with different phase-shifts, frame number and noise (iii) un-predictable performance in practice. To clear these obstacles, we carried out large amount simulations to evaluate the accuracy and convergence of AIA under different conditions and subsequently suggested enhancement of AIA. Condition numbers of least squares matrices used in AIA, $\kappa(\mathbf{A}_{\mathrm{ps}})$ and $\kappa(\mathbf{A}_{\mathrm{p}})$, have been proposed to qualify phase and phase-shifts. Simulations show that AIA cannot perform well when $\kappa(\mathbf{A}_{\mathrm{ps}})$ is large. Hence, we suggest to keep the fringe density above one fringe over ROI to make $\kappa(\mathbf{A}_{\mathrm{ps}})$ close to 2 for the successful application of AIA. Further simulations show that the RMSE of the phase calculated by AIA has a linear relationship w.r.t $\kappa(\mathbf{A}_{\mathrm{p}})^{1/2}$, $M^{-1/2}$ and σ, with which, an integrated error model is fit, and improvements of AIA by controlling phase-shifts and frame numbers and suppressing noise are proposed. As $\kappa(\mathbf{A}_{\mathrm{p}})$, σ and B are unknown in practice, estimation methods of these parameters are presented. Finally, enhanced eAIA is proposed by incorporating all our findings and improvements. An experiment has been carried out to demonstrate the effectiveness of eAIA.

Funding

Economic Development Board - Singapore (S17-1579-IPP-II).

References

1. J. H. Bruning, D. R. Herriott, J. Gallagher, D. Rosenfeld, A. White, and D. Brangaccio, "Digital wavefront measuring interferometer for testing optical surfaces and lenses," Appl. Opt. **13**(11), 2693–2703 (1974).
2. J. E. Greivenkamp, "Generalized data reduction for heterodyne interferometry," Opt. Eng. **23**(4), 234350 (1984).
3. K. Creath, "Phase-measurement interferometry techniques," Prog. Opt. **26**(26), 349–393 (1988).
4. Q. Kemao, Windowed fringe pattern analysis (SPIE Press Bellingham, Wash, USA, 2013).
5. D. Malacara, *Optical shop testing* (John Wiley & Sons, 2007).
6. Y. Surrel, "Design of algorithms for phase measurements by the use of phase stepping," Appl. Opt. **35**(1), 51–60 (1996).

Optics EXPRESS

7. K. Larkin and B. Oreb, "Design and assessment of symmetrical phase-shifting algorithms," J. Opt. Soc. Am. A **9**(10), 1740–1748 (1992).
8. Y. Surrel, "Phase stepping: a new self-calibrating algorithm," Appl. Opt. **32**(19), 3598–3600 (1993).
9. Y. Surrel, "Additive noise effect in digital phase detection," Appl. Opt. **36**(1), 271–276 (1997).
10. P. Carré, "Installation et utilisation du comparateur photoélectrique et interférentiel du Bureau International des Poids et Mesures," Metrologia **2**(1), 13–23 (1966).
11. P. Hariharan, B. Oreb, and T. Eiju, "Digital phase-shifting interferometry: a simple error-compensating phase calculation algorithm," Appl. Opt. **26**(13), 2504–2506 (1987).
12. Z. Wang and B. Han, "Advanced iterative algorithm for phase extraction of randomly phase-shifted interferograms," Opt. Lett. **29**(14), 1671–1673 (2004).
13. J. Vargas, J. A. Quiroga, and T. Belenguer, "Phase-shifting interferometry based on principal component analysis," Opt. Lett. **36**(8), 1326–1328 (2011).
14. J. Deng, H. Wang, D. Zhang, L. Zhong, J. Fan, and X. Lu, "Phase shift extraction algorithm based on Euclidean matrix norm," Opt. Lett. **38**(9), 1506–1508 (2013).
15. J. Vargas, J. A. Quiroga, C. Sorzano, J. Estrada, and J. Carazo, "Two-step demodulation based on the Gram–Schmidt orthonormalization method," Opt. Lett. **37**(3), 443–445 (2012).
16. D. A. Belsley, E. Kuh, and R. E. Welsch, *Regression diagnostics: Identifying influential data and sources of collinearity* (John Wiley & Sons, 2005).
17. D. Zill and J. Dewar, Algebra and Trigonometry (Jones & Bartlett Publishers, 2011).
18. B. N. Parlett, *The symmetric eigenvalue problem* (siam, 1998).
19. J. Nakamura, *Image sensors and signal processing for digital still cameras* (CRC, 2016).
20. C. P. Brophy, "Effect of intensity error correlation on the computed phase of phase-shifting interferometry," J. Opt. Soc. Am. A **7**(4), 537–541 (1990).
21. M. Servin, J. Estrada, and J. A. Quiroga, "The general theory of phase shifting algorithms," Opt. Express **17**(24), 21867–21881 (2009).
22. R. Jozwicki, M. Kujawinska, and L. A. Salbut, "New contra old wavefront measurement concepts for interferometric optical testing," Opt. Eng. **31**(3), 422–434 (1992).
23. Q. Kemao, "Two-dimensional windowed Fourier transform for fringe pattern analysis: principles, applications and implementations," Opt. Laser. Eng. **45**(2), 304–317 (2007).
24. C. Farrell and M. Player, "Phase step measurement and variable step algorithms in phase-shifting interferometry," Meas. Sci. Technol. **3**(10), 953–958 (1992).
25. Q. Kemao, H. Wang, W. Gao, L. Feng, and S. H. Soon, "Phase extraction from arbitrary phase-shifted fringe patterns with noise suppression," Opt. Laser. Eng. **48**(6), 684–689 (2010).
26. G. E. Healey and R. Kondepudy, "Radiometric CCD camera calibration and noise estimation," IEEE Trans. Pattern Anal. Machine Intell. **16**(3), 267–276 (1994).
27. J. Immerkaer, "Fast noise variance estimation," Comput. Vis. Image. Und. **64**(2), 300–302 (1996).